Available online at www.sciencedirect.com
ScienceDirect
Trans. Nonferrous Met. Soc. China 26(2016) 2900−2909
Transactions of Nonferrous Metals Society of China
www.tnmsc.cn

Thermal expansion behavior, microhardness and electrochemical corrosion resistance properties of $Au_{52}Cu_{27}Ag_{17-x}(NiZn_{0.5})_x$ alloys

Ke-chang SHEN[1], Gui-hua LI[2], Wei-min WANG[1]

1. Key Laboratory for Liquid-Solid Structural Evolution and Processing of Materials, Ministry of Education, Shandong University, Ji'nan 250061, China;
2. Shandong Institute of Metrology, Ji'nan 250014, China

Received 24 October 2015; accepted 3 May 2016

Abstract: The thermal expansion behavior, microhardness and electrochemical corrosion resistance of $Au_{52}Cu_{27}Ag_{17-x}(NiZn_{0.5})_x$ (x=0, 6 and 12) alloys were investigated by dilatometer (DIL), microhardness tester, electrochemical workstation, X-ray diffractometer (XRD), scanning electron microscopy (SEM), transmission electron microscopy (TEM) and X-ray photoelectron spectroscopy (XPS). With increasing x, the relative length expansion and DIL maximum temperature $T_{1\,m}$ (i.e., thermal stability) of the alloys increase in thermal expansion measurements, which can be explained by the change of the atomic binding energy, mismatch entropy together with phase transformation. With the increase of x, the microhardness can be improved, but the corrosion resistance decreases; in addition, the anodic peak current densities of polarization curves decrease, which are related closely with the solid solution degree and dissolution of Ag, Ni and Zn alloying elements in Cl^--containing solution.
Key words: gold alloy; thermal expansion; microhardness; corrosion resistance

1 Introduction

Due to good chemical stability, biocompatibility and ductility, the gold is used widely in many fields, such as jewelry industry, dental application and electron component [1−4]. However, the mechanical property of pure gold is relatively poor, which could result in the abrasion and even fracture, hence, alloying is usually used for improving its properties [5,6]. The 18 carat gold composed of 75% Au and 25% master alloys by mass is one of the common gold alloys and is also a popular jewelry gold [7]. The common master alloy elements are Ag, Cu, Ni, Zn, Pd, RE elements, and so on [8,9]. The addition of these alloying elements can improve the processing abilities, mechanical properties and colors of gold alloys.

The essence of thermal expansion is the change of the average lattice spacing with the increase of temperature [10]. Hence, the thermal expansion behavior could reflect the change of lattice structure. In addition, the thermal expansion also is related with some physical properties of alloys, such as heat capacity, binding energy and melting point [11−13]. Through the thermal expansion behavior, the changes of structure and properties of gold alloys with increasing temperature can be analyzed.

The mechanical property, especially the hardness is the most important characteristic of evaluating the quality of gold alloy. It is known that the hardness is related to other mechanical properties closely [1], the improvement of hardness is helpful for enhancing the abrasion resistance and strength of alloy. Although there are some studies on the strengthening mechanism of alloying elements for the hardness of gold alloys, such as solid solution strengthening, precipitation strengthening, grain refinement strengthening, work hardening and aging strengthening [14,15], but the effect of master alloys which contain several alloying elements is still worthy of being explored.

Because of the direct contact with human skins, the corrosion resistance of the 18 carat gold alloy in the sweat environment is necessary to be investigated. The reaction between the gold alloys with sweat could result

Foundation item: Projects (51171091, 51471099, 51571132) supported by the National Natural Science Foundation of China; Project (2012CB825702) supported by the National Basic Research Program of China
Corresponding author: Wei-min WANG; Tel: +86-531-88392749; E-mail: weiminw@sdu.edu.cn
DOI: 10.1016/S1003-6326(16)64419-9

in the discoloration of the alloy [16]. In addition, the release of alloying elements, especially the Ni release could lead to the allergy of skin [17−19]. These are the main disadvantages which hinder the application of gold alloys as the jewelry. Therefore, studying the electrochemical corrosion behavior of 18 carat gold alloys is indispensable for improving the corrosion resistance.

In this study, we chose three 18 carat gold alloys with different master alloy compositions, i.e., the $Au_{52}Cu_{27}Ag_{17-x}(NiZn_{0.5})_x$ (x=0, 6 and 12) alloys with the change of the Ag, Ni and Zn elements contents. The thermal expansion behavior, microhardness and electrochemical corrosion resistance properties were investigated, in order to analyze the effect of master alloys on the properties of 18 carat gold alloys.

2 Experimental

The $Au_{52}Cu_{27}Ag_{17-x}(NiZn_{0.5})_x$ (x=0, 6 and 12) alloys were employed in this study. The pure Au (99.99%) and master alloys (CuAg and CuZnNi) were smelted in crucible by oxygen and acetylene spray gun and then the uniform molten liquid were poured into cast iron mold, after being cooled in the air, the ingots were pressed into thin slices. The compositions of alloys are shown in Table 1.

Table 1 Compositions of $Au_{52}Cu_{27}Ag_{17-x}(NiZn_{0.5})_x$ (x=0, 6 and 12) alloys (mole fraction, %)

x	Au	Cu	Ag	Ni	Zn
0	54.96	28.29	16.75	0	0
6	52.73	27.43	10.82	5.99	3.03
12	50.63	26.97	5.24	11.73	5.43

The samples were investigated by X-ray diffractometer (XRD) with a Cu target (Cu K_α, λ=0.154056 nm). In order to calculate the lattice constant a_0 of phases in alloys, the extended Bragg equation [20] was used as follows:

$$a_0 = \frac{\lambda}{2\sin\theta}\sqrt{h^2+k^2+l^2} \quad (1)$$

where λ is the radiation wavelength, θ is the diffraction angle, and h, k and l are the crystal plane indices.

The morphologies of samples were observed by field emission scanning electron microscopy (SEM, SU−70). The compositions of corresponding regions were analyzed by energy dispersive spectrometer (EDS). Transmission electron microscopy (TEM, JEM−2100) was used to further observe the structure of samples. The TEM specimens were prepared by mechanical thinning to 60 μm and then ion milling. The surface layer elements of samples after electrochemical polarization test were investigated by X-ray photoelectron spectroscopy (XPS, Escalab 250) with monochromatized Al K_α excitation.

The microhardness of each sample was measured for 9 times with 0.05 kg load and 30 s holding time using DHV−1000 digital micro-hardness tester. Thermal expansion curves were measured by a dilatometer (DIL, Netzsch 402C) with a constant heating rate 10 K/min. The lengths of the tested samples were 12.65 mm, 13.58 mm and 13.36 mm, respectively. The potentiodynamic polarization tests with a scanning rate of 5 mV/s at room temperature were carried out by CHI660E advanced electrochemical workstation with a typical three-electrode system in electrochemical measurements: working electrode, platinum counter electrode and $Hg|Hg_2Cl_2$ (SCE) reference electrode. The electrolyte is artificial sweat solution (0.5% NaCl, 0.1% lactic acid and 0.1% urea, adjusted to pH 6.5 with weak aqua ammonia). The artificial sweat was prepared according to GB/T 19719—2005 standard of China, and was used at the temperature of 37 °C.

3 Results

3.1 XRD and TEM results

Figure 1 shows the XRD patterns of samples, as well as the diffraction angles and lattice constants a_0 of (200) peaks. Here, a_0 is calculated by Eq. (1). It can be seen that all samples exhibit similar diffraction peaks which can be nearly assigned to face-center cubic (FCC)

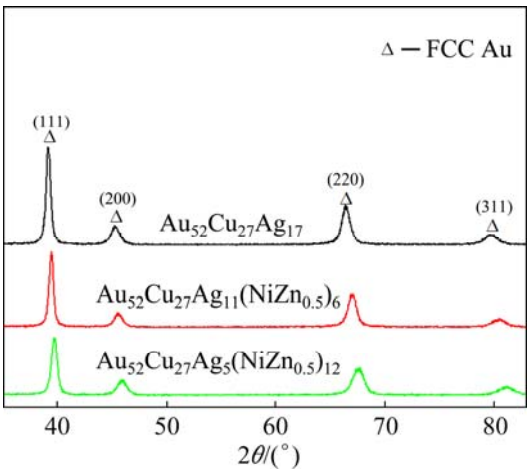

Alloy	2θ/(°)	a_0/nm
Pure Au	44.392	0.4079
$Au_{52}Cu_{27}Ag_{17}$	45.281	0.4002
$Au_{52}Cu_{27}Ag_{11}(NiZn_{0.5})_6$	45.601	0.3975
$Au_{52}Cu_{27}Ag_5(NiZn_{0.5})_{12}$	46.040	0.3940

Fig. 1 XRD patterns of $Au_{52}Cu_{27}Ag_{17-x}(NiZn_{0.5})_x$ (x=0, 6 and 12) alloys, as well as diffraction angles and lattice constants of (200) peaks

crystalline Au structure, and the positions of peaks (2θ) all shift slightly towards the higher diffraction angles with increasing x. According to Eq. (1), a higher diffraction angle represents a lower lattice constant, i.e., the lattice contracts with the increase of x. It is known that Cu, Ag and Ni could form continuous solid solution with Au [21,22], Zn can be soluble in Cu and Ni solid solutions. In addition, there are no apparent peaks of intermetallic compounds detected in XRD patterns due to their low contents. Therefore, it can be thought that the alloys are mainly constituted by the Au solid solution. The atom radius of Ag is similar to that of Au, so the lattice distortion caused by Ag is not obvious. The higher shifts of peak positions can be ascribed to the obvious smaller atom radius of Cu, Ni and Zn atoms which could replace some Au atoms in structure and shorten the distance between atoms [23−25].

The TEM images and corresponding selected area electron diffraction patterns (SAED) of $Au_{52}Cu_{27}Ag_{17}$ and $Au_{52}Cu_{27}Ag_5(NiZn_{0.5})_{12}$ alloys are shown in Fig. 2. The bright field images show that the $Au_{52}Cu_{27}Ag_5(NiZn_{0.5})_{12}$ alloy is more easily thinned, and there are some particles on the surface of both alloys. Based on the identified lattice, it can be found that the compositions of both alloys are mainly Au phase, while in $Au_{52}Cu_{27}Ag_5(NiZn_{0.5})_{12}$ alloy, some intermetallic compounds are demarcated more easily. The SAED patterns further verify the coexistence of Au solid solution and some intermetallic compounds in alloys, which is consistent with XRD results (Figs. 1 and 2).

3.2 Thermal expansion and microhardness

Figure 3 exhibits the thermal expansion (DIL) curves and corresponding coefficients of thermal expansion (CTE) curves of three samples. T_{lm} and T_{cm} respectively represent the DIL maximum temperature and CTE maximum temperature, and the T_{lm} points can also be thought as the inflection points of the thermal expansion curves. All the thermal expansion curves rise with increasing temperature and the relative length expansions ($\Delta L/L_0$) increase with increasing x, which can be thought as the linear thermal expansion stages before the inflection points. While after the respective inflection point, the thermal expansion curves all have a decline trend. It also can be found that the T_{lm} and T_{cm} both increase with increasing x. Since, the increase of x reflects the enhancement of solid solubility, there should be some links between the thermal expansion behavior and the solid solubility (Figs. 1 and 3).

The coefficient of thermal expansion (α) which is defined as fractional change in length per unit change in temperature can be expressed by the following equation [26,27]:

$$\alpha = \frac{\Delta L}{L_0 \times \Delta T} \tag{2}$$

where L_0 is the length of tested sample, ΔL is the thermal expansion increment of sample when temperature variation value is ΔT. The average coefficient of thermal expansion ($\bar{\alpha}$) is shown in Fig. 4(a), it is obvious that the $\bar{\alpha}$ increases with increasing x. With regard to the

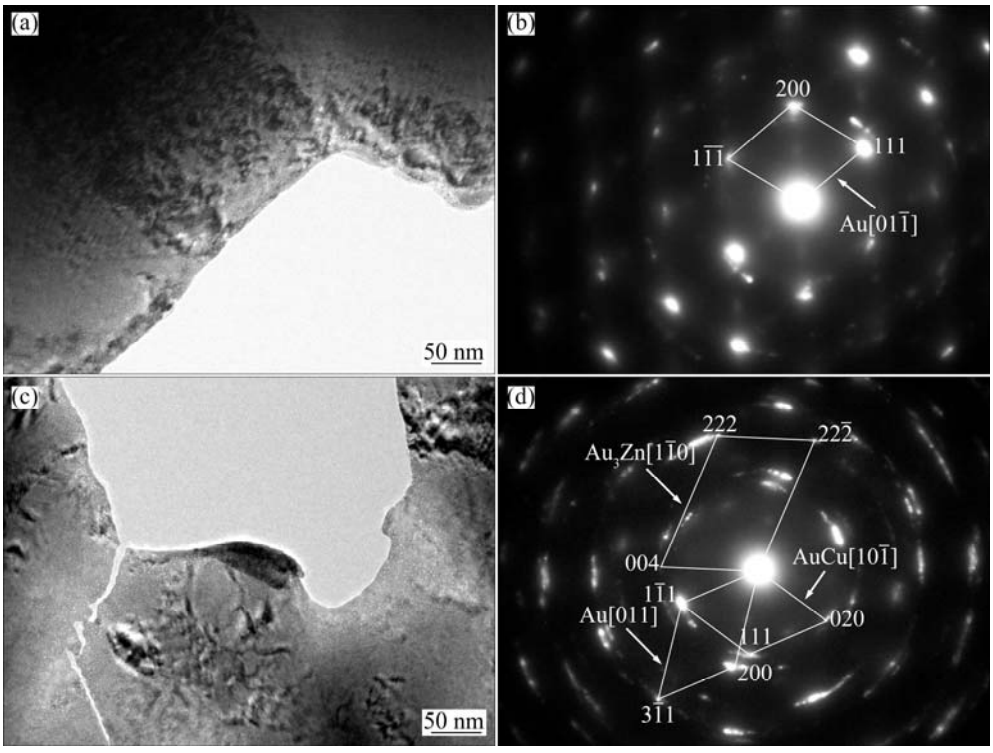

Fig. 2 TEM images and corresponding SAED patterns of $Au_{52}Cu_{27}Ag_{17-x}(NiZn_{0.5})_x$ alloys: (a, b) x=0; (c, d) x = 12

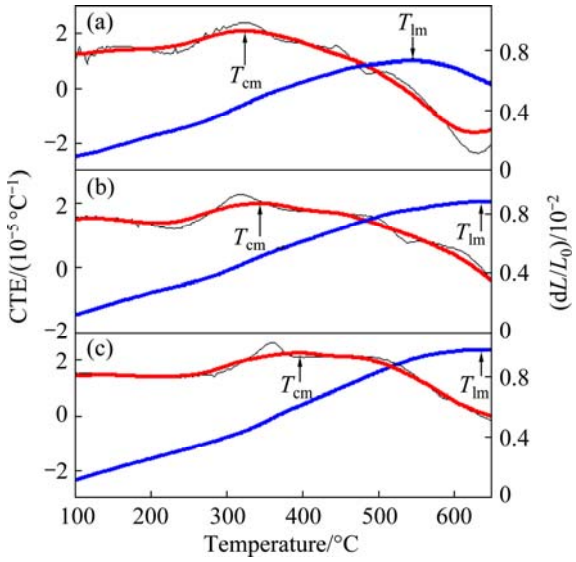

Fig. 3 Thermal expansion curves (blue line) and experimental coefficients of thermal expansion (CTE) curves (red line) of $Au_{52}Cu_{27}Ag_{17-x}(NiZn_{0.5})_x$ (x=0, 6 and 12) alloys

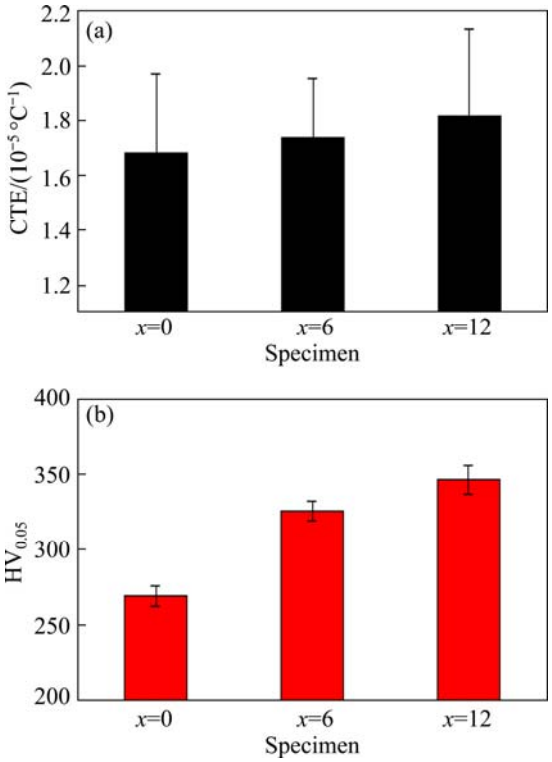

Fig. 4 Average coefficient of thermal expansion ($\bar{\alpha}$) of range of 100 °C to T_{cm} (a) and microhardness of $Au_{52}Cu_{27}Ag_{17-x}(NiZn_{0.5})_x$ (x=0, 6 and 12) alloys (b)

CTE curve which is usually used for expressing the effect of thermal expansion phenomenon on alloy [28], it can be seen that in the early stage, the curves of all samples keep nearly steady, and then after rise to their maximums at T_{cm} points, they begin to decline with increasing temperature.

The microhardness histograms of samples are shown in Fig. 4(b). It can be seen apparently that the $Au_{52}Cu_{27}Ag_{17}$ alloy exhibits the lowest microhardness, while $Au_{52}Cu_{27}Ag_5(NiZn_{0.5})_{12}$ alloy exhibits the largest one, i.e., the microhardness values of samples increase with increasing x.

3.3 Potentiodynamic polarization

Figure 5 shows the potentiodynamic polarization curves tested in the artificial sweat solution. All the polarization curves exhibit the similar shapes, suggesting the same electrochemical corrosion behaviors. It can be seen that the corrosion potential (φ_{corr}) of the $Au_{52}Cu_{27}Ag_{17}$ alloy is the highest among three samples, and that of the $Au_{52}Cu_{27}Ag_5(NiZn_{0.5})_{12}$ alloy is the lowest. On the contrary, the corrosion current density (J_{corr}) of the $Au_{52}Cu_{27}Ag_{17}$ alloy is the lowest, while that of the $Au_{52}Cu_{27}Ag_5(NiZn_{0.5})_{12}$ alloy is the highest. Therefore, it can be thought that the corrosion resistance abilities of the alloys get worse with increasing x. It also can be noticed that the width of passivation ranges of alloys are nearly equal, while the passivation current densities increase with increasing x, which implies that higher x of the alloys results in worse stabilities of passive films. Therefore, the passivation current densities also indicate a worse corrosion resistance ability of the alloy which has a higher x.

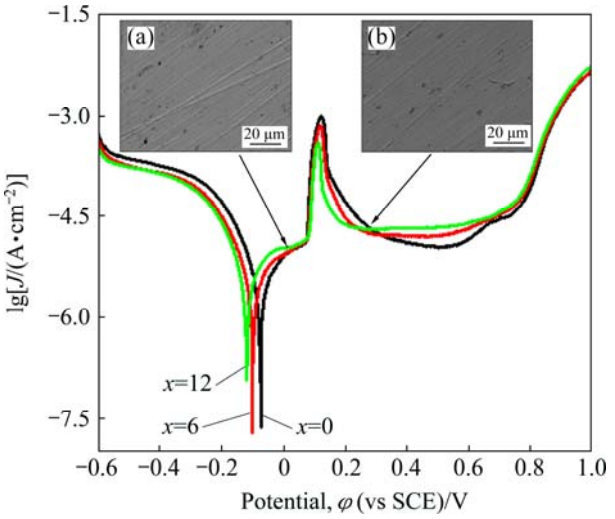

Fig. 5 Potentiodynamic polarization curves of $Au_{52}Cu_{27}Ag_{17-x}(NiZn_{0.5})_x$ (x=0, 6 and 12) alloys in artificial sweat solution (The insets are the SEM images of the alloys before (a) and after (b) the anodic current peaks)

Moreover, the peaks of all polarization curves appear which can be defined as anodic current peaks before the broad passivation ranges. The corresponding potentials and current densities of the peaks are listed in Table 2. It can be found that with increasing x, the peak potentials and current densities decrease. In addition, the

insets of Fig. 5 are the SEM images of samples of which the polarization measurement was stopped before and after the appearance of the peaks, respectively. However, the surface morphologies are not obviously different between the samples obtained before and after the peaks.

Table 2 Potentials and current densities of anodic current peaks deduced from potentiodynamic polarization curves

Alloy	Potential/V	Current density/ (10^{-4}A·cm^{-2})
$Au_{52}Cu_{27}Ag_{17}$	0.122	9.687
$Au_{52}Cu_{27}Ag_{11}(NiZn_{0.5})_6$	0.119	6.988
$Au_{52}Cu_{27}Ag_5(NiZn_{0.5})_{12}$	0.112	3.948

Figure 6 exhibits the XPS spectra which could reflect the variation of elements of the $Au_{52}Cu_{27}Ag_5(NiZn_{0.5})_{12}$ alloy surfaces before and after the peaks, while the corresponding binding energies (E_B) are listed in Table 3. It can be seen that compared to the samples before the peaks, there are some changes of the XPS spectra of the samples after the peaks. According to the XPS spectra and E_B (Fig. 6 and Table 3), the electronic structure of Au 4f before and after current peak can both be thought as the coexistence of Au^0 and Au^+ [29] (Fig. 6(a)). The E_B of Cu 2p is corresponding to the Cu^+ [30] (Fig. 6(b)), and the E_B of Ag 3d characterizes the coexistence of Ag^0 and Ag^+ [4,31] (Fig. 6(c)). Accordingly, the E_B of Ni 2p represents the

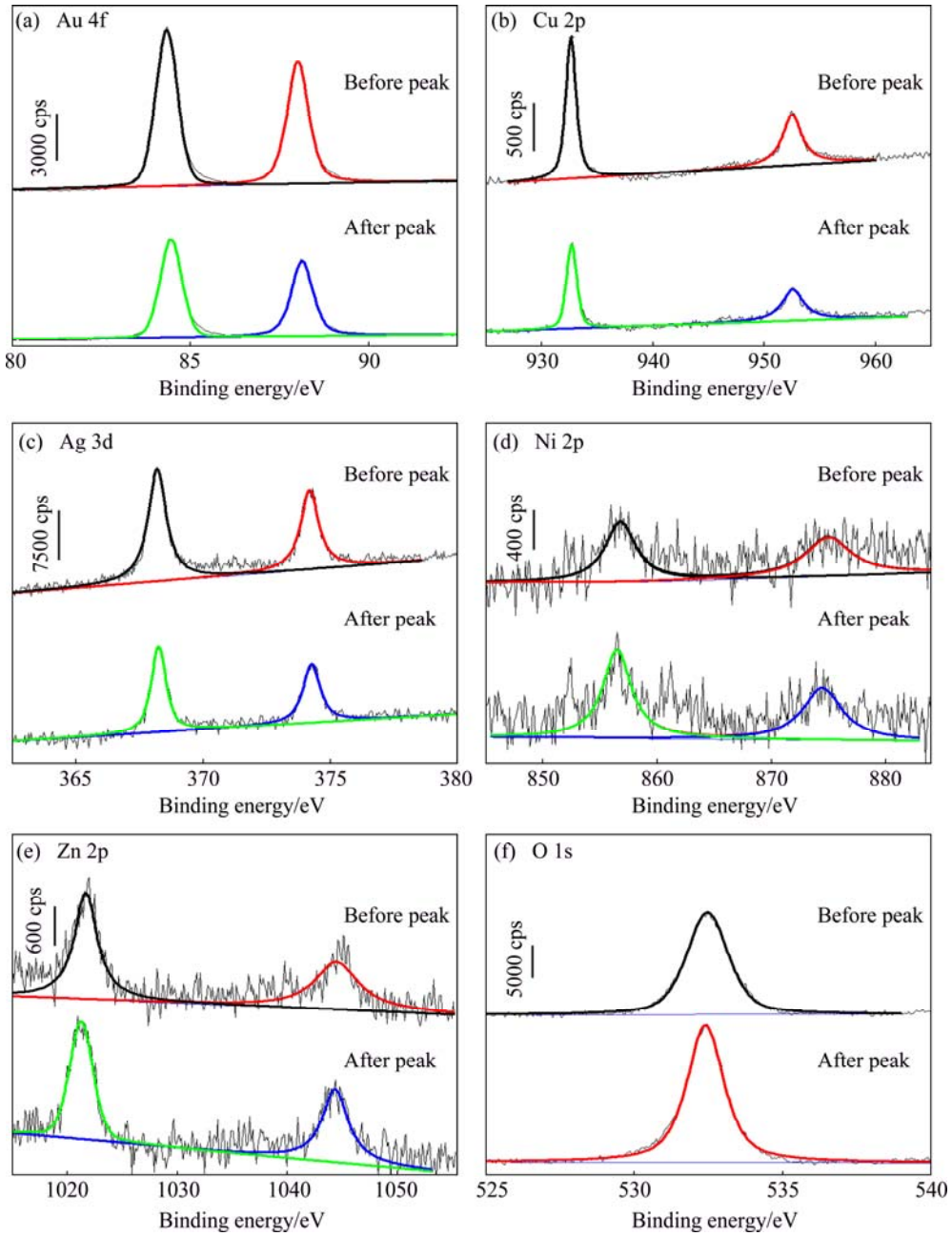

Fig. 6 XPS spectra of $Au_{52}Cu_{27}Ag_5(NiZn_{0.5})_{12}$ alloys before and after anodic current peaks of polarization curves tested in artificial sweat solution

Table 3 Binding energies (E_B) of elements before anodic peak (E_{B1}) and after anodic peak (E_{B2}) deduced from XPS spectrum

Element	E_{B1}/eV	E_{B2}/eV	ΔE_B/eV
Au 4f	84.34	84.46	0.12
	88.02	88.14	0.12
Cu 2p	932.67	932.73	0.06
	952.52	952.59	0.07
Ag 3d	368.20	368.26	0.06
	374.19	374.27	0.08
Ni 2p	856.81	856.51	−0.30
	875.97	874.48	−1.49
Zn 2p	1021.71	1021.29	−0.42
	1044.51	1044.37	−0.14
O 1s	532.47	532.40	−0.07

$\Delta E_B=E_{B_2}-E_{B_1}$

existence of Ni^{2+} and Ni^{3+} [32], and that of Zn 2p represents the Zn^{2+} [33] (Figs. 6(d) and (e)). The ΔE_B shows that compared with the samples before anodic current peak, the E_B of Au, Cu and Ag of samples after the peaks shift towards the higher values and those of Ni, Zn and O of samples after the peaks become lower (Table 3).

Figure 7 shows the SEM morphologies of the alloys after being tested in artificial sweat solution by polarization curve measurements. It can be found that the pits of the $Au_{52}Cu_{27}Ag_5(NiZn_{0.5})_{12}$ alloy are more than that of the $Au_{52}Cu_{27}Ag_{17}$ alloy, which can also prove that the higher x results in worse corrosion resistance. Some white particles disperse on both sample surfaces. According to the corresponding EDS results, the contents of Au, Cu, Ni and Zn in the matrix are higher than those in the particle, while the Ag content in the particle is much higher than that in the matrix and the Cl elements can be found only in the particles. Hence, the particles may be constituted mainly by AgCl due to the measurement in the Cl^--containing solution. In addition, Fig. 8 shows the SEM morphologies of $Au_{52}Cu_{27}Ag_{17}$ and $Au_{52}Cu_{27}Ag_5(NiZn_{0.5})_{12}$ alloys which were eroded by the mixture solution of HCl and HNO_3 (V_{HCl} : V_{HNO_3} = 1:1). It is apparent that the pits of $Au_{52}Cu_{27}Ag_5(NiZn_{0.5})_{12}$ alloy are much larger than that of $Au_{52}Cu_{27}Ag_{17}$ alloy, which is in accordance with the above results that the corrosion resistance of the alloy decreases with increasing x. However, there are some particles dispersed on the samples, and the particles of $Au_{52}Cu_{27}Ag_{17}$ alloy are much more than that of $Au_{52}Cu_{27}Ag_5(NiZn_{0.5})_{12}$ alloy. According to the EDS results, the Au and Cu contents of the matrix are higher than those of particles, while the contents of Ag, Ni and Zn of the matrix are lower than those of particles. Especially, the Ag content of particles is apparently higher than that of the matrix, and the Ag contents as well as the particles both decrease with increasing x, hence, it can be thought that these particles may be the corrosion products which are mainly composed of Ag element.

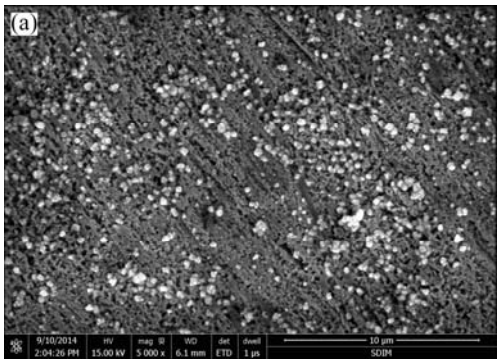

	Mole fraction/%			
	Au	Cu	Ag	Cl
Matrix	56.8	29.8	13.4	
Particle	41.4	20.0	26.1	12.4

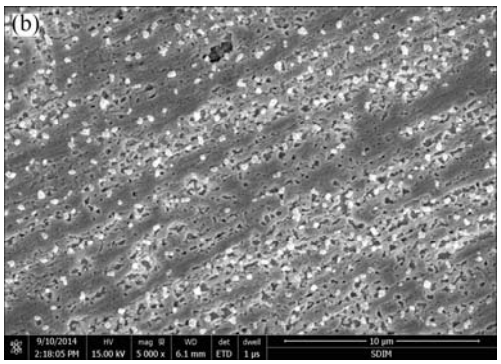

	Mole fraction/%					
	Au	Cu	Ag	Ni	Zn	Cl
Matrix	53.7	25.2	3.5	12.2	5.4	
Particl	40.9	14.6	23.6	6.4	4.7	9.8

Fig. 7 SEM images and EDS results of $Au_{52}Cu_{27}Ag_{17-x}(NiZn_{0.5})_x$ ((a) x=0, (b) x=12) alloys after full polarization in artificial sweat solution

4 Discussion

4.1 Thermal expansion behavior of $Au_{52}Cu_{27}Ag_{17-x}(NiZn_{0.5})_x$ (x=0, 6 and 12) alloys

It is known that mixing enthalpy is related with the expansion of the solid solutions [34,35]. Table 4 shows the mixing enthalpy (ΔH_{mix}), the mismatch entropy normalized by the Boltzmann constant (S_σ/k_B) and the relative length expansion ($\Delta L/L_0$). The ΔH_{mix} and S_σ/k_B were calculated by the following equations [36]:

$$\Delta H^{chem}=\sum_{\substack{i=1\\ i\neq j}}\Omega_{ij}c_ic_j \tag{3}$$

$$\frac{S_\sigma}{k_B}=\frac{3}{2}(\zeta^2-1)y_1+\frac{3}{2}(\zeta-1)^2y_2-$$

$$\left[\frac{1}{2}(\zeta-1)(\zeta-3)+\ln\zeta\right](1-y_3) \quad (4)$$

$$y_1=\frac{1}{\sigma_3}\sum_{j>i=1}(d_i+d_j)(d_i-d_j)^2c_ic_j \quad (5)$$

$$y_2=\frac{\sigma^2}{(\sigma_3)^2}\sum_{j>i=1}d_id_j(d_i-d_j)^2c_ic_j \quad (6)$$

$$y_3=\frac{(\sigma^2)^3}{(\sigma^3)^2} \quad (7)$$

$$\sigma^k=\sum_{i=1}c_i{d_i}^k;k=2,3 \quad (8)$$

where Ω_{ij} is the regular solution interaction parameter between the i and j elements, and c_i is the atomic mole fraction of the i element. ζ is defined as $\zeta=1/(1-\xi)$ with a packing fraction ξ which is fixed to be 0.64. y_1, y_2 and y_3 are dimensionless parameters and they have a relation: $y_1+y_2+y_3=1$. d_i is the atomic diameter. It can be seen that the lower the master alloy content x, the more negative the ΔH_{mix} as well as the lower $\Delta L/L_0$ (Table 4). However, the ΔH_{mix} could reflect the binding energies [37], hence, a lower x value represents a higher binding energy which implies the lower $\Delta L/L_0$. As mentioned above, it can be thought that the substitution of Ni and Zn atoms with Au atoms results in the weakening of the binding energy in the FCC solid solution matrix [38]. Therefore, the higher the x value, the higher the $\Delta L/L_0$ during the heating processes (Fig. 3 and Table 4).

Table 4 Mixing enthalpy (ΔH_{mix}), mismatch entropy normalized by Boltzmann constant (S_σ/k_B) and relative length expansion ($\Delta L/L_0$) of alloy during thermal expansion measurement

Alloy	ΔH_{mix}/(kJ·mol^{-1})	S_σ/k_B	$\Delta L/L_0$
$Au_{52}Cu_{27}Ag_{17}$	−7.40	0.061	0.731
$Au_{52}Cu_{27}Ag_{11}(NiZn_{0.5})_6$	−5.87	0.069	0.880
$Au_{52}Cu_{27}Ag_5(NiZn_{0.5})_{12}$	−4.70	0.078	0.980

The change of CTE may reflect the variation of the structure during the heating process like the phase transformation $\alpha\rightarrow\gamma$ transformations in Fe−C alloys [39,40]. Generally, the increase of the temperature can influence the solubility of the matrix phase and result in the phase transformations [41,42]. Analogously, the contraction of the alloy in this study may be related with the solid solubility changes and phase transformations during heating process. In fact, for Au−Cu−Ag system, with the increase of the temperature, the solid solubility would increase [43,44]. Hence, the more Ni and Zn atoms will substitute Au atoms, which could result in the shrinkage of lattice (Fig. 1). In addition, the AuCu phases which have been detected by SAED measurement in tested alloys (Fig. 2) can generate order−disorder transition with increasing temperature, i.e., the order AuCu phase could change into a disorder structure [40,45,46]. As mentioned above, the contraction of the alloy during heating process can be ascribed to the changes of solid solubility and phase transformation.

In addition, the S_σ/k_B increases with increasing x (Table 4), and a higher mismatch entropy could represent a more difficulty of phase transformation. Hence, with increasing x, the increase trend of DIL maximum temperature T_{lm}, corresponding to the increase of phase transformation temperature which means the improvement of thermal stability of the alloy, can be ascribed to the variation of the mismatch entropy.

4.2 Microhardness and solid solubility of $Au_{52}Cu_{27}Ag_{17-x}(NiZn_{0.5})_x$ alloys

It is known that the solid solution strengthening stems from the restriction of dislocation movement caused by the interaction of dislocation with the distorted lattice surrounding the solute atoms [47]. Commonly, with the increase of the amount of solute atoms in solid solution, the improvement of the strength of alloy is expected [48]. The variation of x represents the decrease of Ag content and the increase of Ni and Zn contents in structure of the alloy (Table 1). However, Ni can enhance the mechanical performance of the alloy [17,49]. The following equation is often used for the estimate of the solid solution strengthening effects of alloy elements on the Au-based alloy [15]:

$$H_s=A\cdot B \quad (9)$$

where A and B represent the atomic mass ratio and the atomic radius difference between Au and alloying atom, respectively. A higher H_s indicates a larger lattice distortion which could result in a better solid solution effect. Being calculated by Eq. (9), the H_s of Ag, Ni and Zn are 0.004, 0.443 and 0.230, respectively. It is apparent that the Ni and Zn atoms have much higher H_s than Ag atom. In fact, due to the similar atomic mass and radius to that of Au, the Ag atom has weak solid solution strengthening effect. According to XRD results, the main compositions of all alloys are FCC solid solutions. With increasing the x, a higher shift of peak position, i.e., a larger deviation with the pure Au diffraction peak, indicates a higher solid solubility (Fig. 1). Hence, the solid solution strengthening can be considered as the main strengthening mechanism in this study. The increase of Ni and Zn can improve the hardness of the alloy, while the decrease of Ag content has a weak effect on the solid solution strengthening for Au (Fig. 4(b)).

4.3 Electrochemical polarization behavior of $Au_{52}Cu_{27}Ag_{17-x}(NiZn_{0.5})_x$ (x = 0, 6 and 12) alloys

It can be seen from the Au−Ni binary alloy phase diagram, the solid state separation into Au-rich and Ni-rich phases occurs below 821 °C [50]. The same phase decomposition also occurs in Au−Cu−Ni ternary alloy and Au−Cu−Ni−Zn alloy in the similar manner [51]. Hence, the higher x may imply the higher content of Ni-rich phases in the tested alloy. It is known that the standard electrode potential φ^0 (vs SHE) of electrochemical reaction $Au=Au^{3+}+3e$ is 1.50 V (SHE represents the reference electrode of standard hydrogen electrode), while that of electrochemical reaction $Ni=Ni^{2+}+2e$ is −0.250 V [52]. Therefore, it is expected that the corrosion potentials φ_{corr} and corrosion resistance decrease with increasing x (Fig. 5), which is similar to the results in Ref. [17].

According to the Refs. [53,54], the formation of the anodic current peak can be ascribed to the oxidation of alloying elements, i.e., the active dissolution process. Usually, for most transition metals, a higher E_B represents a higher oxidation state, while Ag is one of the few metals which exhibit the lower E_B in the oxidation state [55]. Hence, it is indicated that the degrees of oxidation of Au and Cu of samples after current peaks are higher than that of samples before current peaks, while the degrees of oxidation of Ag, Ni and Zn have the opposite change tendency (Fig. 6 and Table 3). Meanwhile, the electrode potentials of Ag, Ni and Zn are lower than that of Au, but the degrees of oxidation of Ag, Ni and Zn shift towards the lower values rather than the higher values after the peaks. Since the dissolution can result in the decrease of the oxide on the sample surfaces, i.e., the oxide degree decreases, therefore, the dissolution of Ag, Ni and Zn can be thought as the main reason why the oxidation degrees of these elements of the samples surfaces decline. As mentioned above, the anodic current peaks of polarization curves of the alloys can be ascribed to the oxidation of the surface elements, especially the dissolution of the Ag, Ni and Zn.

Since the Ag content in the corrosion products is higher than those of Ni and Zn (Fig. 8). In the solution contained Cl^-, the alloy with a higher Ag content may be easily corroded and more corrosion products arise. Therefore, the difference of current density may be related to the variation of Ag content, i.e., a lower Ag content results in a lower anodic current peak (Fig. 5 and Table 2).

5 Conclusions

1) The relative length expansion and DIL maximum temperature T_{lm} (i.e., thermal stability) of $Au_{52}Cu_{27}Ag_{17-x}(NiZn_{0.5})_x$ (x=0, 6 and 12) alloys increase with increasing x, which are ascribed to the weakening of the atomic binding energy and rise of the mismatch entropy together with phase transformation, respectively. The solid solution strengthening of Ni and Zn atoms due to their small atomic weight and radius is the main reason why the microhardness of the alloys increases and their lattice constant a_0 decreases with increasing x.

2) The corrosion resistance of the alloy decreases with increasing x due to the increase of Ni-rich phase which has the lower corrosion potential than Au-rich phase. The appearance of anodic current peak is ascribed to the dissolution of alloy elements, such as Ag, Ni and Zn. In addition, the higher the x, the lower the anodic current peak, which is caused by the dissolution of Ag element in Cl^--containing solution.

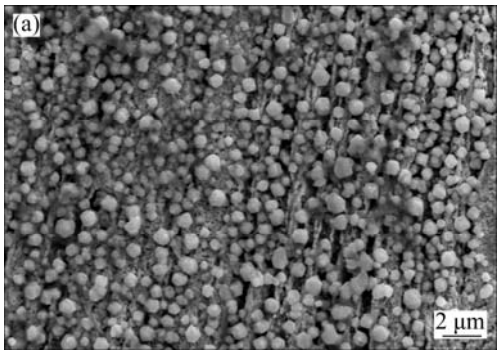

	Mole fraction/%		
	Au	Cu	Ag
Matrix	51.2	19.3	29.4
Particle	40.5	4.5	55.0

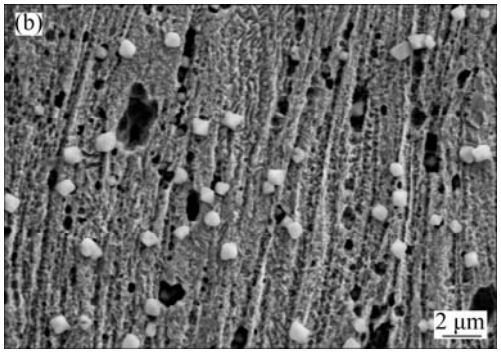

	Mole fraction/%				
	Au	Cu	Ag	Ni	Zn
Matrix	58.7	25.2	7.1	9.0	
Particle	46.3	11.4	28.3	11.0	2.9

Fig. 8 SEM images and EDS results of $Au_{52}Cu_{27}Ag_{17-x}(NiZn_{0.5})_x$ ((a) x=0, (b) x=12) alloys after immersion in mixture solution of hydrochloric and nitric acid (V_{HCl}:V_{HNO_3}=1:1)

References

[1] LEE H K, MOON H M, SEOL H J, LEE J E, KIM H I. Age

hardening by dendrite growth in a low-gold dental casting alloy [J]. Biomaterials, 2004, 25(17): 3869−3875.

[2] BUENCONSEJO P J S, LUDWIG A. New Au−Cu−Al thin film shape memory alloys with tunable functional properties and high thermal stability [J]. Acta Materialia, 2015, 85: 378−386.

[3] XU C, SRITHARAN T, MHAISALKAR S G, SRINIVASAN M, ZHANG S. An XPS study of Al_2Au and $AlAu_4$ intermetallic oxidation [J]. Applied Surface Science, 2007, 253(14): 6217−6221.

[4] WANG Jing, SONG Da-qian, WANG Li-ying, ZHANG Hua, ZHANG Han-qi, SUN Ying. Design and performances of immunoassay based on SPR biosensor with Au/Ag alloy nanocomposites [J]. Sensors and Actuators B Chemical, 2011, 157(2): 547−553.

[5] CORTI C W. Metallurgy of microalloyed 24 carat golds [J]. Gold Bulletin, 1999, 32(2): 39−47.

[6] XIE Xin-lin, ZHANG Lei, XIAO Jin-kun, QIAN Zhi-yuan, ZHANG Tao, ZHOU Ke-chao. Sliding electrical contact behavior of AuAgCu brush on Au plating [J]. Transactions of Nonferrous Metals Society of China, 2015, 25(9): 3029−3036.

[7] KURTOĞLU A, TUĞRUL A B. Gold analysis by the gamma absorption technique [J]. Applied Radiation and Isotopes, 2003, 58(1): 5−8.

[8] O'CONNOR G P. Alloying additions for 18 carat white gold jewelry alloys [J]. Metals Technology, 1979, 6(1): 261−266.

[9] GUSMANO G, MONTANARI R, MONTESPERELLI G, TATA M E, BEMPORAD E, VALENTE M, KACIULIS S, MATTOGNO G. Influence of Si, Ni and Co additions on gold alloy for investment cast process [J]. Journal of Alloys and Compounds, 2001, 325(1): 252−258.

[10] CHEN Yan, LIU Lin, WANG Yue-hui, LIU Jian-hua, ZHANG Rui-jun. Microstructure evolution and thermal expansion of Cu−Zn alloy after high pressure heat treatment [J]. Transactions of Nonferrous Metals Society of China, 2011, 21(10): 2205−2209.

[11] CHEN Ying, IWATA S, MOHRI T. First-principles calculation of phase equilibria and phase separation of the Fe−Ni alloy system [J]. Rare Metals, 2006, 25(5): 437−440.

[12] JUNG D Y, KUROSAKI K, KIM C E, MUTA H, YAMANAKA S. Thermal expansion and melting temperature of the half-Heusler compounds: MNiSn (M=Ti, Zr, Hf) [J]. Journal of Alloys and Compounds, 2010, 489(2): 328−331.

[13] HAYASHI H, KANOH M, QUAN C J, INABA H, WANG S R, DOKIYA M, TAGAWA H. Thermal expansion of Gd-doped ceria and reduced ceria [J]. Solid State Ionics, 2000, 132(3−4): 227−233.

[14] NING Yuan-tao. Microalloying of gold and gold alloys [J]. Precious Metals, 2008, 29(2): 55−61.

[15] YANG Qing-qing, XIONG Wei-hao, ZHANG Jie. Study on strengthening mechanism of Au990-Ti jewelry alloys [J]. Rare Metal Materials and Engineering, 2006, 35(12): 1904−1907.

[16] RAPSON W S. Tarnish resistance, corrosion and stress corrosion cracking of gold alloys [J]. Gold Bulletin, 1996, 29(2): 61−69.

[17] YUAN Jun-ping, LI Wei, LIU Wen-ming. Nickel release rate of 18 KW gold alloy for ornaments [J]. Rare Metals, 2013, 32(1): 33−39.

[18] RIZZI P, CORAZZARI I, FIORE G, FENOGLIO I, FUBINI B, KACIULIS S, BATTEZZATI L. Ion release and tarnishing behavior of Au and Pd based amorphous alloys in artificial sweat [J]. Corrosion Science, 2013, 77: 135−142.

[19] LIU Na, LI Zhou, LI Ling, LIU Bin, XU Gen-ying. Processing map and hot deformation mechanism of novel nickel-free white copper alloy [J]. Transactions of Nonferrous Metals Society of China, 2014, 24(11): 3492−3499.

[20] ZHOU Yu, WU Gao-hui. Materials analysis and testing technology [M]. Harbin: Harbin Institute of Technology Press, 2007. (in Chinese)

[21] CHUDNENKO K V, PAL'YANOVA G A. Thermodynamic properties of solid solutions in the Ag−Au−Cu system [J]. Russian Geology and Geophysics, 2014, 55(3): 349−360.

[22] YANG Tao, RAMASAMY D, QUEIR S R P, LOUREIRO F J A, de ALMEIDA C M R, JULI O P S. The annealing influence on the microstructure and performance of Au@Ni core-shell bimetal as the cathode of low-temperature solid oxide fuel cells [J]. International Journal of Hydrogen Energy, 2015, 40(14): 4980−4988.

[23] YANG Tao, de ALMEIDA C M R, RAMASAMY D, LOUREIRO F J A. A detailed study of Au−Ni bimetal synthesized by the phase separation mechanism for the cathode of low-temperature solid oxide fuel cells [J]. Journal of Power Sources, 2014, 269: 46−53.

[24] KIM H H, MOON J J, HEO Y W, LEE H S. Effect of thermal annealing on Ni/Au contact to a-InGaZnO films deposited by dc sputtering [J]. Thin Solid Films, 2010, 518(22): 6348−6351.

[25] WANDEKAR R V, WANI B N, BHARADWAJ S R. Crystal structure, electrical conductivity, thermal expansion and compatibility studies of Co-substituted lanthanum strontium manganite system [J]. Solid State Sciences, 2009, 11(1): 240−250.

[26] MAIENSCHEIN J L, GARCIA F. Thermal expansion of TATB-based explosives from 300 to 566 K [J]. Thermochimica Acta, 2002, 384(1): 71−83.

[27] SU C H, FETH S, LEHOCZKY S L. Thermal expansion coefficient of ZnSe crystal between 17 and 1080 °C by interferometry [J]. Materials Letters, 2009, 63(17): 1475−1477.

[28] ZIYA A B, OHSHIMA K. X-ray diffraction study of the structure and thermal parameters of the ternary Au−Ag−Pd alloys [J]. Journal of Alloys and Compounds, 2006, 425(1−2): 123−128.

[29] WANG Chuan-xi, XU Lin, XU Xiao-wei, CHENG Hao, SUN Hong-chen, LIN Quan, ZHANG Chi. Near infrared Ag/Au alloy nanoclusters: tunable photoluminescence and cellular imaging [J]. Journal of Colloid and Interface Science, 2014, 416: 274−279.

[30] SOBCZAK I, WOLSKI Ł. Au−Cu on Nb_2O_5 and Nb/MCF supports–Surface properties and catalytic activity in glycerol and methanol oxidation [J]. Catalysis Today, 2015, 254: 72−82.

[31] GERENSER L J. Photoemission investigation of silver/poly(ethylene terephthalate) interfacial chemistry: The effect of oxygen-plasma treatment [J]. Journal of Vacuum Science & Technology A: Vacuum, Surfaces, and Films, 1990, 8(5): 3682−3691.

[32] OLSZEWSKA D. Application of XPS method in the research into Ni ion-modified montmorillonite as a SO_2 sorbent [J]. Fuel Processing Technology, 2012, 95: 90−95.

[33] LI Yan, ZHANG Bo-ping, ZHAO Jin-xian. Enhanced photocatalytic performance of Au−Ag alloy modified ZnO nanocomposite films [J]. Journal of Alloys and Compounds, 2014, 586: 663−668.

[34] SHVAREVA T Y, ALEXANDROV V, ASTA M, NAVROTSKY A. Energetics of mixing in ThO_2−CeO_2 fluorite solid solutions [J]. Journal of Nuclear Materials, 2011, 419(1−3): 72−75.

[35] BONNY G, PASIANOT R C, MALERBA L, CARO A, OLSSON P, LAVRENTIEV M Y. Numerical prediction of thermodynamic properties of iron–chromium alloys using semi-empirical cohesive models: The state of the art [J]. Journal of Nuclear Materials, 2009, 385(2): 268−277.

[36] TAKEUCHI A, INOUE A. Calculations of mixing enthalpy and mismatch entropy for ternary amorphous alloys [J]. Materials Transactions Jim, 2000, 41(11): 1372−1378.

[37] YANG Hong-wei. Study on thermodynamic model of enthalpy of mixing of liqiud alloys [D]. Kunming: Kunming University of Science and Technology, 2012. (in Chinese)

[38] KIM S H, KIM H S, LEE Y W, SOHN D S, SUHR D S. Variation of the lattice parameter and thermal expansion coefficient of $(U,Dy)O_2$ as a function of $DyO_{1.5}$ content [J]. Journal of Alloys and Compounds, 2006, 407(1−2): 263−267.

[39] LIU Y C, SOMMER F, MITTEMEIJER E J. The austenite–ferrite

transformation of ultralow-carbon Fe−C alloy; transition from diffusion- to interface-controlled growth [J]. Acta Materialia, 2006, 54(12): 3383−3393.

[40] ANRAKU T, SAKAIHARA I, HOSHIKAWA T, TANIWAKI M. Phase transitions and thermal expansion behavior in AuCu alloy [J]. Materials Transactions, 2009, 50(3): 683−688.

[41] HISATSUNE K, SAKRANA A, HAMASAKI K, HERNANDEZ R, SALONGA J P. Phase transformation in a dental gold alloy for soldering [J]. Journal of Alloys and Compounds, 1997, 261(1): 308−312.

[42] LEE Jae-ho, YI Sang-joon, SEOL Hyo-joung, KWON Yong-hoon, LEE Jai-bong, KIM Hyung-il. Age-hardening by metastable phases in an experimental Au−Ag−Cu−Pd alloy [J]. Journal of Alloys and Compounds, 2006, 425(1−2): 210−215.

[43] PRINCE A. Critical assessment of copper-gold-silver ternary system [J]. International Materials Reviews, 1988, 33(1): 314−338.

[44] CHATTERJEE K, HOWE J M, JOHNSON W C, MURAYAMA M. Static and in situ TEM investigation of phase relationships, phase dissolution, and interface motion in Ag−Au−Cu alloy nanoparticles [J]. Acta Materialia, 2004, 52(10): 2923−2935.

[45] KLAY E, DIOLOGENT F, ARN ODO J, DUBOS P, MORTENSEN A. Solid state transformations of Au−Cu−Pt alloys studied by in-situ X-ray synchrotron radiation and DSC [J]. Intermetallics, 2011, 19(5): 726−737.

[46] XIE You-qing, LIU Xin-bi, LI Xiao-bo, PENG Hong-jian, NIE Yao-zhuang. Holographic alloy positioning design system and holographic network phase diagrams of Au−Cu system [J]. Transactions of Nonferrous Metals Society of China, 2015, 25(3): 885−906.

[47] HYUN S M, KRAFT O, VINCI R P. Mechanical behavior of Pt and Pt−Ru solid solution alloy thin films [J]. Acta Materialia, 2004, 52(14): 4199−4211.

[48] ROBERTI R, CORNACCHIA G, FACCOLI M, GELFI M. On the strengthening mechanisms of 18 carat yellow gold and its mechanical behaviour [J]. Materials Science and Engineering A, 2008, 488(1−2): 50−54.

[49] HENDERSON S, MANCHANDA D. White gold alloys: Color measurement and grading [J]. Gold Bulletin, 2005, 38(2): 55−67.

[50] NORMANDEAU G. White golds: A review of commercial material characteristics & alloy design alternatives [J]. Gold Bulletin, 1992, 25(3): 96−103.

[51] YUAN Jun-ping, LI Wei, WANG Chang. Nickel release of 10 K white gold alloy for jewelry [J]. Rare Metal Materials and Engineering, 2012, 41(6): 947−951.

[52] CAO Chu-nan. Principle of corrosion electrochemistry [M]. Beijing: Chemical Industry Press, 2004. (in Chinese)

[53] LIN J C, CHAN J Y. On the resistance of silver migration in Ag−Pd conductive thick films under humid environment and applied d.c. field [J]. Materials Chemistry and Physics, 1996, 43(3): 256−265.

[54] ZADOROZNE N, REBAK R, GIORDANO M, ARES A, CARRANZA R. Effect of temperature and chloride concentration on the anodic behavior of nickel alloys in bicarbonate solutions [J]. Procedia Materials Science, 2012, 1: 207−214.

[55] QU Zhen-ping, KE Guo-zhou, WANG Yi, LIU Meng-wei, JIANG Ting-ting, GAO Jin-suo. Investigation of factors influencing the catalytic performance of CO oxidation over Au−Ag/SBA-15 catalyst [J]. Applied Surface Science, 2013, 277: 293−301.

$Au_{52}Cu_{27}Ag_{17-x}(NiZn_{0.5})_x$ 合金的热膨胀行为、显微硬度和电化学耐腐蚀性能

神克常[1]，李桂华[2]，王伟民[1]

1. 山东大学 材料液固结构演变与加工教育部重点实验室，济南 250061；
2. 山东省计量科学研究院，济南 250014

摘　要：利用热膨胀仪(DIL)、显微硬度计、电化学工作站、X 射线衍射仪(XRD)、扫描电子显微镜(SEM)、透射电子显微镜(TEM)、X 射线光电子能谱(XPS)研究了 $Au_{52}Cu_{27}Ag_{17-x}(NiZn_{0.5})_x$ (x=0, 6，12)合金的热膨胀行为、显微硬度和电化学耐腐蚀性。随着 x 的增加，在热膨胀实验测试中合金的相对长度膨胀量和 DIL 曲线极大值的温度 T_{lm}(即热稳定性)增加，这可以归因于原子结合能、错配熵的变化以及相变。增加 x，合金的显微硬度可以得到提高，但是耐腐蚀性下降；此外，极化曲线的阳极电流峰密度随着 x 的增加而下降，这些结果与固溶度以及 Ag、Ni、Zn 合金元素在含 Cl^-离子溶液中的溶解密切相关。

关键词：金合金；热膨胀；显微硬度；耐腐蚀性

(Edited by Yun-bin HE)